Thank you for reviewing our revised manuscript. Below are the reviewers' comments (in black) and our responses (in green).

Reviewer 1:

I am pleased with most changes that have been made to the manuscript.

I have two remaining concerns.

One is figure 10. Per my request, it had been changed it to display four different regions rather than the original altitude layers, but when these new results were inconclusive, the figure was reverted to height layers. Having looked at the original altitude plot, it seems to me that in terms of the Re distribution, only the highest altitude layer was significantly distinct from the rest. For the version of this figure that showed geographic regions instead, the authors noted that the 180-120W DJF area had a broader size distribution than did 60E-120E JJA, which was a region characterized by more frequent convection. The unique characteristics of the other regions were less conclusive.

I would like to see key impacts of altitude and geography combined into one plot. This could be accomplished different ways, but for example: an upper panel could have all TTL clouds below 16.5 km, the other could be only TTL clouds from 16.5-17.5 km (from the original figure), and the two lower panels could show 180-120W DJF and 60E-120E JJA, respectively, to highlight differences in the distribution (broad versus narrow) with respect to convective activity focused in these areas. As before, I think it is useful to see the number of samples included within each layer or region.

We have remade Figure 10 to contain clouds in (a) 14.5 to 16.5km, (b) 16.5 to 17.5 km, (c) 120E-180E DJF, and (d) 60E-120E JJA. The latter two are regions likely to be influenced by convection as discussed in the paper. The discussion on r_e (lines 279-296) has been modified according to this new figure.

The other concern came out in my back and forth with Aurelian (the other reviewer) about the numbering of wave phases. Upon review, I realize the sequence originally came from the K16 paper (specifically their figure 5) and the current manuscript is consistent with theirs in this regard. While I believe the sequence in K16 is illogical as it stands -- phase 3 and phase 4 results ought to have been swapped – I'm not going to require any change here, for the sake of consistency with K16, and because the adoption of any particular numbering sequence is done by convention.

Thanks for your comments regarding the naming convention. We agree that would make more sense to swap phase 3 and 4, but we will keep the current convention to facilitate comparison with K16.

Reviewer 2:

I am satisfied with the authors response to the reviewers' comments and recommend publication of the paper. I have included below two further formulation suggestions for the authors to consider before final publication.

line 271 'the confinement in Phase 1 may be positioned closer to Phase 2' → 'the region of confinement may overlap with both Phase 1 and 2, with its center still inside Phase 1 but closer to Phase 2.'

Changed as suggested.

line 295: 'were situated closer Phase 2.' → I preferred the initial phrasing. I would suggest something like: 'were situated closer to the T minimum so that ice crystals were moving around between Phase 1 and 2.'

Changed as suggested.

Influence of gravity wave temperature anomalies and their vertical gradients on cirrus clouds in the tropical tropopause layer – a satellite-based view

Kai-Wei Chang[1] and Tristan L'Ecuyer[2]

[1]Department of Atmospheric Sciences, Texas A&M University, College Station, Texas, USA
[2]Department of Atmospheric and Oceanic Sciences, University of Wisconsin-Madison, Madison, Wisconsin, USA

Correspondence: Kai-Wei Chang (kchang37@wisc.edu)

Abstract.

Negative temperature perturbations (T') from gravity waves are known to be favorable to tropical tropopause layer (TTL) clouds, and recent studies have further suggested a possible role of dT'/dz on facilitating TTL cloud formation and maintenance. With a focus on exploring the influence of dT'/dz on TTL clouds, this study utilizes radio occultation temperature retrievals and cloud layers from the Cloud-Aerosol Lidar and Infrared Pathfinder Satellite Observations (CALIPSO) to understand how gravity wave perturbations modulate cloud occurrence in the tropics.

Cloud populations were evaluated in four phases corresponding to positive or negative T' and dT'/dz. We find that 55% of TTL clouds are found where T' and dT'/dz are both negative. Regions of frequent convection are associated with higher cloud populations in the warm phase $T' > 0$. We show that the partitioning of cloud population among wave phases exhibit dependence on background relative humidity. In the phase where T' and dT'/dz are both negative, the mean cloud effective radius is the smallest of all four phases, but the differences are small.

It is shown that the strongest mean negative T' anomaly is centered on the cloud top, resulting in positive dT'/dz above the cloud top and negative dT'/dz below. This negative T' anomaly propagates downward with time, characteristic of upward propagating gravity waves. Negative (positive) T' anomalies are associated with increased (decreased) probability of being occupied by clouds. The magnitude of T' correlates with the increase or decrease in cloud occurrence, giving evidence that the wave amplitude influences the probability of cloud occurrence. While the decrease of cloud occurrence in the warm phase is centered on the altitude of T' maxima, we show that the increase of cloud occurrence around T' minima occurs below the minima in height, indicating that cloud formation or maintenance is facilitated mainly inside negative dT'/dz. Together with existing studies, our results suggest that the cold phase of gravity waves is favorable to TTL clouds mainly through the region where dT'/dz is negative.

1 Introduction

Variations in stratospheric water vapor (SWV) influence the rate of surface warming due to climate change (Solomon et al., 2010) and have a significant climate feedback (Banerjee et al., 2019). There is a need to better understand mechanisms controlling the amount of SWV, as they are potentially key components of climate change and stratosphere-troposphere coupling. Since the large-scale slow upwelling throughout the tropical tropopause layer (TTL) brings air from the troposphere into the lower stratosphere, conditions and processes in the TTL modulate the amount of water vapor in the lower tropical stratosphere. Cirrus formation by cold temperatures in the TTL is generally regarded as the primary mechanism dehydrating air entering the stratosphere (Holton et al., 1995). Studies have shown that cirrus cloud occurrence strongly associates with Kelvin waves (Immler et al., 2007; Fujiwara et al., 2009) and gravity waves (Suzuki et al., 2013; Kim et al., 2016), and that these waves can enhance the dehydration occurring inside the TTL (Schoeberl et al., 2015).

Previous studies on waves and cirrus clouds generally show that enhanced cirrus cloud occurrence tend to coincide with the gravity wave phases with negative temperature anomalies. Through aircraft observations of the NASA Airborne Tropical TRopopause EXperiment (ATTREX) campaign (Jensen et al., 2013), Kim et al. (2016) (K16 hereafter) show that ice was found most frequently where the temperature anomaly (T') and vertical gradient of temperature anomalies (dT'/dz) were both negative, bringing the latter quantity into attention as a possible control on cirrus formation. Since K16 showed that the occurrence of convectively-coupled clouds had no preference towards the sign of T' or dT'/dz, the tendency of TTL clouds to exist in negative T' and dT'/dz likely depicts a connection between clouds and gravity wave perturbations. They suggest that the negative rate of change in temperature (positive cooling rate) in regions where $dT'/dz < 0$, due to the downward phase propagation of gravity waves, may facilitate cloud formation and explain the abundance of cloud in the phase with $T' < 0$ and $dT'/dz < 0$. Another explanation of high cloud frequency in this phase is given by Podglajen et al. (2018) (P18 hereafter) who used a simplified set of equations to model the interaction between ice crystal growth, sedimentation, and gravity wave perturbations of temperature and vertical motion. P18 argues that in this phase the upward vertical motion acts in concert with the sedimentation rate of ice crystals with certain sizes, suspending crystals inside this wave phase as it descends with the downward phase propagation of the wave. Since $dT'/dz < 0$ corresponds to a upward vertical wind anomaly, this result supports the presence of ice in negative T' and dT'/dz. Motivated by these studies, we aim to further explore this connection between gravity waves and cirrus clouds through satellite datasets.

This study utilizes temperature profiles from the radio occultation (RO) technique (Kursinski et al., 1997) which has been widely used to study equatorial gravity and Kelvin waves (Randel and Wu, 2005; Alexander et al., 2008; Scherllin-Pirscher et al., 2017). We collocate these RO profiles to cirrus cloud observations from the Cloud-Aerosol Lidar and Infrared Pathfinder Satellite Observations (Winker et al., 2010) to study the relationship between gravity/Kelvin wave phases and cirrus occurrence. Especially within 2007 to 2013 there is a high spatial and temporal density of RO soundings from the U.S.-Taiwan joint mission Constellation Observing System for Meteorology, Ionosphere, and Climate (COSMIC) (Anthes et al., 2008), allowing a large number of RO profiles to be collocated with cirrus cloud retrievals.

Collocations that are temporally close in time are used to evaluate wave perturbations T' and dT'/dz in relation to cloud occurrence and properties. In addition, since the sampling of COSMIC is pseudo-random in both space and time, it is possible to obtain RO profiles that are spatially close to CALIPSO footprints but before or after the time of the footprint. Using collocations of various time separations we build composite time series of wave anomalies and cloud frequency to understand how waves are influencing TTL clouds. Finally, we use the Aura Microwave Limb Sounder (MLS) water vapor retrievals (Read et al., 2007) and ice cloud effective radius (r_e) retrievals from the CloudSat/CALIPSO 2C-ICE product (Deng et al., 2013, 2015) to evaluate whether relative humidity and r_e are related to gravity waves as shown by P18.

Section 2 describes the datasets used in this study. In Section 3 we explain the extraction of wave temperature anomalies from RO profiles and the method for data collocation. In Section 4, results are given in three parts: Section 4.1 discusses the population of clouds in each wave phase, Section 4.2 presents the composite time evolution of wave anomalies and cloud frequecy, and Section 4.3 evaluates the predictions of P18 with satellite observations. Our conclusions are summarized in Section 5.

2 Satellite products

This study uses the re-processed radio occultation (RO) atmPrf dataset processed by the Cosmic Data Analysis and Archive Center (CDAAC). We use occultations from the following satellite missions: Constellation Observation System for Meteorology, Ionosphere, and Climate (COSMIC) (Anthes et al., 2008), Meteorological Operational Polar Satellite A/Global Navigation Satellite System Receiver for Atmospheric Sounding (Metop-A/GRAS) (Von Engeln et al., 2009), Metop-B/GRAS, and the Challenging Minisatellite Payload (CHAMP) (Wickert et al., 2001). Because the RO technique does not suffer from inter-satellite calibration effects (Foelsche et al., 2011), profiles from different satellite missions can be used together as long as they are processed with the same algorithm. The level 2 atmPrf dataset provides 'dry' profiles of atmospheric temperature derived by neglecting moisture, which is appropriate for TTL altitudes. The atmPrf provides temperature estimates at 30-meter vertical spacing, but the effective resolution of RO is around 200 meters in the tropical tropopause layer (Zeng et al., 2019). The precision of temperature is approximately 0.5 K within 8 to 20 km (Anthes et al., 2008).

The Cloud-Aerosol Lidar and Infrared Pathfinder Satellite Observations (CALIPSO) (Winker et al., 2010) is a sun-synchronus, polar-orbiting satellite along the NASA A-Train formation, passing the equator at 0130 and 1330 local solar time. Its primary instrument, the Cloud-Aerosol Lidar with Orthogonal Polarization (CALIOP), is a dual-wavelength lidar capable of detecting subvisual clouds with optical depths less than 0.01. We use the Level 2 V4.10 5-km Cloud Layer product for estimates of cloud top and base altitude and the V4.10 5-km Cloud Profile product for detection of clouds in 60-meter vertical bins. The Cloud Aerosol Discrimination (CAD) score in these products is a measure of confidence that the detected feature is correctly classified as cloud. To ensure high confidence that all analyzed features are clouds, our analysis only includes CALIPSO layers and bins with CAD score of 80 or higher (where 100 means complete confidence in the feature being a cloud). Corresponding to the dates when RO data were available, we use nighttime CALIPSO data between 2007 and 2013. Daytime CALIPSO data were excluded due to the lower signal-to-noise ratio of daytime CALIOP observations.

Estimates of ice cloud effective radius (r_e) come from the 2C-ICE product (Deng et al., 2013, 2015) which is derived jointly using the CloudSat radar and CALIPSO lidar observations. This product provides r_e retrievals at 1-km footprints in 250-m vertical bins. The r_e estimates from 2C-ICE compare well to in-situ flight measurements with a mean retrieval-to-flight ratio of 1.05 (Deng et al., 2013). For quality control, we only use r_e with uncertainty (given by the re_uncertainty variable) less than 20%. Due to a battery failure CloudSat left the A-Train formation in 2011. After that it only operated in daytime and its footprint was no longer collocated to CALIPSO. For this reason we limit our analysis using 2C-ICE to 2007 to 2010 when nighttime data was available.

The Aura MLS H_2O product provides retrievals of water vapor mixing ratio at pressures at and below 316 hPa with a precision of 0.2-0.3 ppmv (4-9%) in the stratosphere (Lambert et al., 2007). We use the water vapor mixing ratio to estimate relative humidity with respect to ice (RH_i) using collocated RO temperature. Criteria for data screening follows all the recommendations outlined in section 3.9 of the product documentation (Livesey et al., 2017). Although Aura was launched in 2004, the scan of the MLS did not align with that of CALIOP until May 2008. For this reason, all analysis involving this product is limited to 2008 to 2013.

3 Methods

3.1 Gravity wave temperature anomalies

Our method for obtaining temperature perturbations (T') due to gravity waves is based on Alexander et al. (2008). Mean temperature profiles are calculated on grid boxes of 20° longitude × 5° latitude × 7 days centered on each day of year. Mean maps are made for each day between 1 Jan 2007 and 31 December 2013 during which COSMIC provided a large number of RO observations. For an arbitrary RO temperature profile, the mean map centered on the same day as the RO profile is used to derive the corresponding mean-state profile through bilinear interpolation of the four grid boxes surrounding the location of the given RO profile. T' is then obtained by removing the mean state from the actual profile. Since we use a 7-day mean state, the resulting T' can be thought of as representing variability on timescales less than seven days. After T' is obtained, its vertical gradient is calculated to get dT'/dz. Figure 1 shows one example of a temperature profile, its corresponding mean state, and the resulting anomalies T' and dT'/dz.

3.2 Collocation of CALIPSO observations to RO profiles

The primary goal of this work is to study cirrus occurrence and properties in the four gravity wave phases defined in Figure 1. To accomplish this we collocate CALIPSO cloud observations to RO temperature profiles. The horizontal weighting of RO retrievals is mostly centered within 200 to 300 km of the perigee (tangent) point (Kursinski et al., 1997) where the ray experiences most bending. For this reason we use the spatial location of the perigee point as basis for collocation. Since our interest lies strictly inside the TTL and the perigee point of each occultation ray changes with height, we determine the perigee point at the middle of the TTL by interpolating the longitude and latitude of RO profiles to 17.25 km (middle of TTL determined

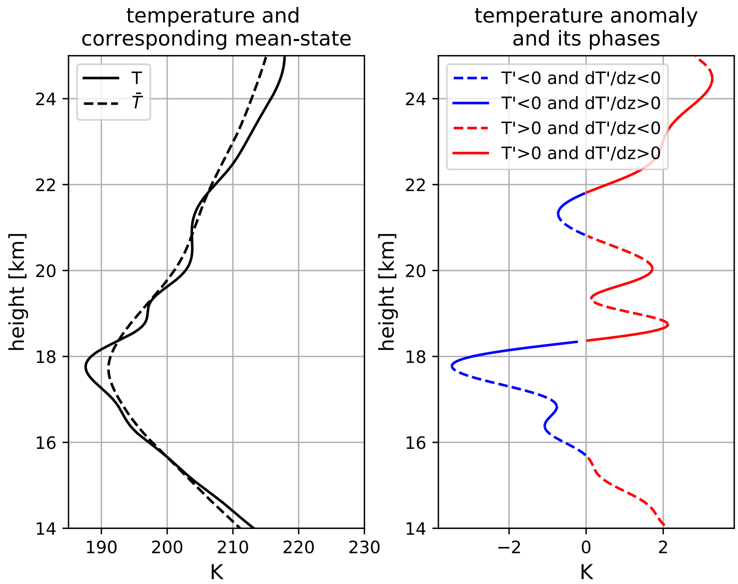

Figure 1. (Left) Temperature profile (solid line) from COSMIC at 155° 43′ W, 18° 16′ N on 1 Jan 2007 and its corresponding mean-state (dashed). (Right) T' of the given profile and its four phases based on the sign of T' and dT'/dz.

as the average of 14.5 km and 20 km). Any CALIPSO observations within 100 km of this point are collocated to the RO profile for analysis. Figure 2 gives an example of one RO profile, its perigee point at 17.25 km, and the collocated CALIPSO 5-km footprints.

We collocate RO profiles to 2C-ICE cloud retrievals in a similar manner. Unlike the CALIPSO 5-km products, 2C-ICE provides cloud properties at 1-km footprints and vertical bins of approximately 250 m. Other than this difference, the collocation method is identical to that of CALIPSO and RO. In May 2008 the Aura MLS was aligned to within ± 10 km of CALIOP. For analysis involving RH_i, for each CALIPSO footprint with a RO collocation, we find the closest MLS footprint to that CALIPSO footprint to calculate RH_i.

4 Results

All results below were derived from data within 20° of the equator. For convenience we will refer to the four gravity wave phases as follows. Phase 1: $T' < 0$ and $dT'/dz < 0$; Phase 2: $T' < 0$ and $dT'/dz > 0$; Phase 3: $T' > 0$ and $dT'/dz < 0$; and Phase 4: $T' > 0$ and $dT'/dz > 0$. Cold and warm phases refer to where $T' < 0$ and $T' > 0$, respectively.

For the analysis presented in Section 4.1 and Section 4.3, the temporal restriction for collocation is that all the collocated data must be within two hours of each other. This restriction is not imposed in 4.2, and the time difference between RO and CALIPSO observations range from 0 to 36 hours with the purpose of examining how waves and cirrus clouds tend to evolve over time. This will be further elaborated in that section.

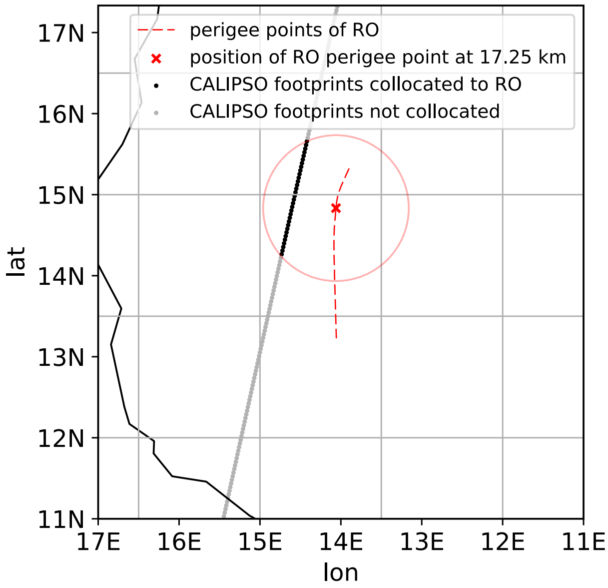

Figure 2. Schematic of collocation between RO profile and CALIPSO footprints. The perigee points of the RO profile throughout all altitudes are shown in the red dashed line, while the position of the perigee point in the middle of the TTL (17.25 km) is denoted by the red X. The CALIPSO 5-km product provides estimates of cloud properties at 5-km footprints, and all footprints within 100 km of the red X are collocated with the RO profile, as indicated by the black dots. Gray dots are CALIPSO footprints are considered too far from the RO profile and not collocated. The shown RO profile was taken at approximately 0120UTC 2 Jan 2009.

4.1 Population of clouds in wave phases

As previously mentioned, K16 (their Figure 5) found that a majority of TTL clouds in the ATTREX data were observed in the cold phase $T' < 0$ and that in the 2014 flight legs over the Western Pacific there was a higher frequency of ice inside $dT'/dz < 0$ than in $dT'/dz > 0$. To assess whether this tendency is general throughout the TTL or is limited to the regions observed by ATTREX, we evaluate cloud populations using collocated CALIPSO and RO observations that cover the TTL at all longitudes and over 2007–2013. Figure 3 shows the population of CALIPSO Cloud Profile vertical bins detected as clouds in each wave phase extracted from collocated RO profiles. Considering all collocated observations between 1 January 2007 and 31 December 2013, 54.9% of clouds are observed to occur in Phase 1 throughout the entire TTL, as shown in Figure 3(a). When the cloud population is examined in 1-km vertical layers (14.5–15.5 km, 15.5–16.5 km, etc.), there is no obvious change with height and most clouds are found in Phase 1 followed by Phase 2 at all heights. Above 16.5 km there is a smaller fraction of clouds in the warm phase. A possible explanation for this may be that there are less convectively detrained clouds as altitude increases, increasing the probability of clouds having been formed by gravity waves. In addition, the population in Phase 2 tends to increase with height, with 38% of clouds above 17.5 km in Phase 2. For comparison, using K16's Figure 5 one can infer that for clouds above 16.5 km the cloud fraction in Phase 1, 2, 3, and 4 are 56.25%, 31.25%, 9.375%, and 3.125%

(calculated as the percentage in that phase divided by the sum all four phases), and for clouds below 16 km the percentages are 49.30%, 28.17%, 14.08%, and 8.45%. These ratios are similar to our findings, though we find less clouds in Phase 2 below 16 km. While the percentages in Figure 3(a) are representative of the entire tropics, the above estimates based on K16's Figure 5 are based on observations over the Western Pacific. We split the tropics into smaller regions to facilitate better comparison.

Cloud fractions in each phase are separated into six longitudinal belts in Figure 4. Filled bars represent the cloud fraction of all TTL clouds while unfilled bars represent only clouds above the mean tropopause of their respective season and longitudinal belt. During December-January-February (DJF), the 120°E-180°E belt, which covers the Maritime Continent and Western Pacific, has the lowest cloud population in Phase 1 (51%) as well as the most clouds inside the warm phase (24%). Although this region is known for very low tropopause temperatures and high TTL cirrus frequency during DJF (Highwood and Hoskins, 1998; Sassen et al., 2009), there is also frequent deep convection (Ramage, 1968) which may generate clouds unrelated to gravity waves. This may explain the higher cloud population in warm phases. By eliminating clouds below the tropopause, above which convective detrainment is rare, the amount of clouds inside the warm phase in this region reduces to 10%.

The influence of convection may also explain the high warm phase population during June-July-August (JJA) in 60°E-120°E where there is frequent convection due to the Asian summer monsoon. In this period and region, 28% of clouds are in the warm phase and 47% are in Phase 1. However, the reduction of cloud population in the warm phase after eliminating clouds below the tropopause is not as apparent here. One possible cause of this may be that the tropopause within 10°N to 40°N is elevated due to the Asian monsoon anticyclone in the upper troposphere, causing the tropopause to be more than 1 km higher than the zonal mean (Ploeger et al., 2015). Since our mean tropopause is calculated based on all profiles within 20°N to 20°S, some clouds from convective detrainment (especially those in the Northern Hemisphere) may still be included in the cloud population.

Over 180°W-120°W, which approximately covers the Eastern Pacific, 56% (25%) of clouds fall in Phase 1 (Phase 2) during DJF . This is in contrast with K16 who found that in the 2011 and 2013 ATTREX flight legs over the Eastern Pacific there were slightly more clouds in Phase 2 than in Phase 1. The 2011 flights were conducted in October and November while the 2013 flights were in February and March. Plots similar to Figure 4 made from data in October-November (not shown) yielded Phase 1/2 populations of 64%/23% while February-March yielded 57%/20%. Over this region we were not able to find Phase 2 having more clouds as K16 did. Their T' were calculated as the difference between aircraft in-situ temperature and 30-day mean temperature derived from RO, while we calculate it as the difference between RO-derived temperatures and 7-day mean profiles. Reproducing the cloud population using 31-day mean temperature as the background still resulted in more clouds in Phase 1 than 2 (not shown). It is not clear what causes this difference.

Using the cloud top and base heights reported from the CALIPSO Cloud Layer product we calculate the cloud fraction in each wave phase, defined as the amount of vertical overlap between individual cloud layers and wave phases in Figure 1. For example, if a phase layer occupies 15.0 to 16.0 km and the CALIPSO product reports a cloud layer extending from 15.2 to 15.7 km, then the cloud fraction would be 0.5. The cloud fraction of each observed wave phase is evaulated, and the resulting distributions of cloud fraction are shown in Figure 5. In this figure and table we only consider clouds with base above 14.5 km and wave phase layers whose base height lie within 14.5 and 18.5 km. Note that cloud fractions of 0 and 1 are excluded in this

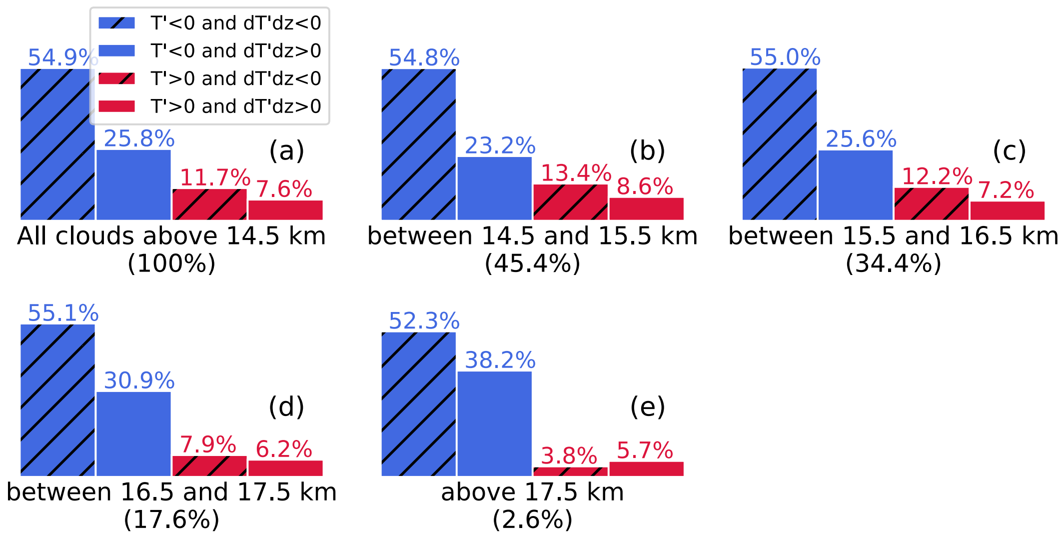

Figure 3. Population of CALIPSO Cloud Profile cloud bins inside each wave phase from 1 January 2007 to 31 December 2013. Plot (a) shows the cloud population for all of TTL (14.5 to 20 km), while (b)–(e) show the population in three different 1-km layers. The percentage in parenthesis denote the portion of clouds found in that vertical layer relative to all TTL clouds.

figure. Corresponding to Figure 5, the total sample number in each phase is shown in the first column of Table 1, while the number of cases with unity cloud fraction is shown in the second column.

In phases of positive dT'/dz, the number of samples tend to decrease as cloud fraction increases. This trend doesn't apply for negative dT'/dz, and in Phase 1 there is a clear increase of samples with increasing cloud fraction. In contrast, Phase 2 and 4 tends to have smaller cloud fractions, while Phase 3 has a rather uniform distribution across all values. It is interesting that Phase 3 has high percentage (43%) of unity cloud fraction, much higher than Phase 4. Although both Phase 3 and 4 both have positive temperature anomaly, we find that Phase 3 seems to be much more favorable for clouds, consistent with P16's assertion that upward vertical wind anomaly is an important factor in maintaining ice clouds.

Table 1. Number of cases with cloud fraction (CF) between 0 and 1 (sum of cases in Figure 5), and CF = 1. The percentage represents the number of CF=1 cases over the sum of the respective row.

Wave Phase	0<CF<1	CF=1
Phase 1	30,519	19,410 (38.9%)
Phase 2	32,152	10,656 (24.9%)
Phase 3	12,687	9,583 (43.0%)
Phase 4	9,784	999 (9.3%)

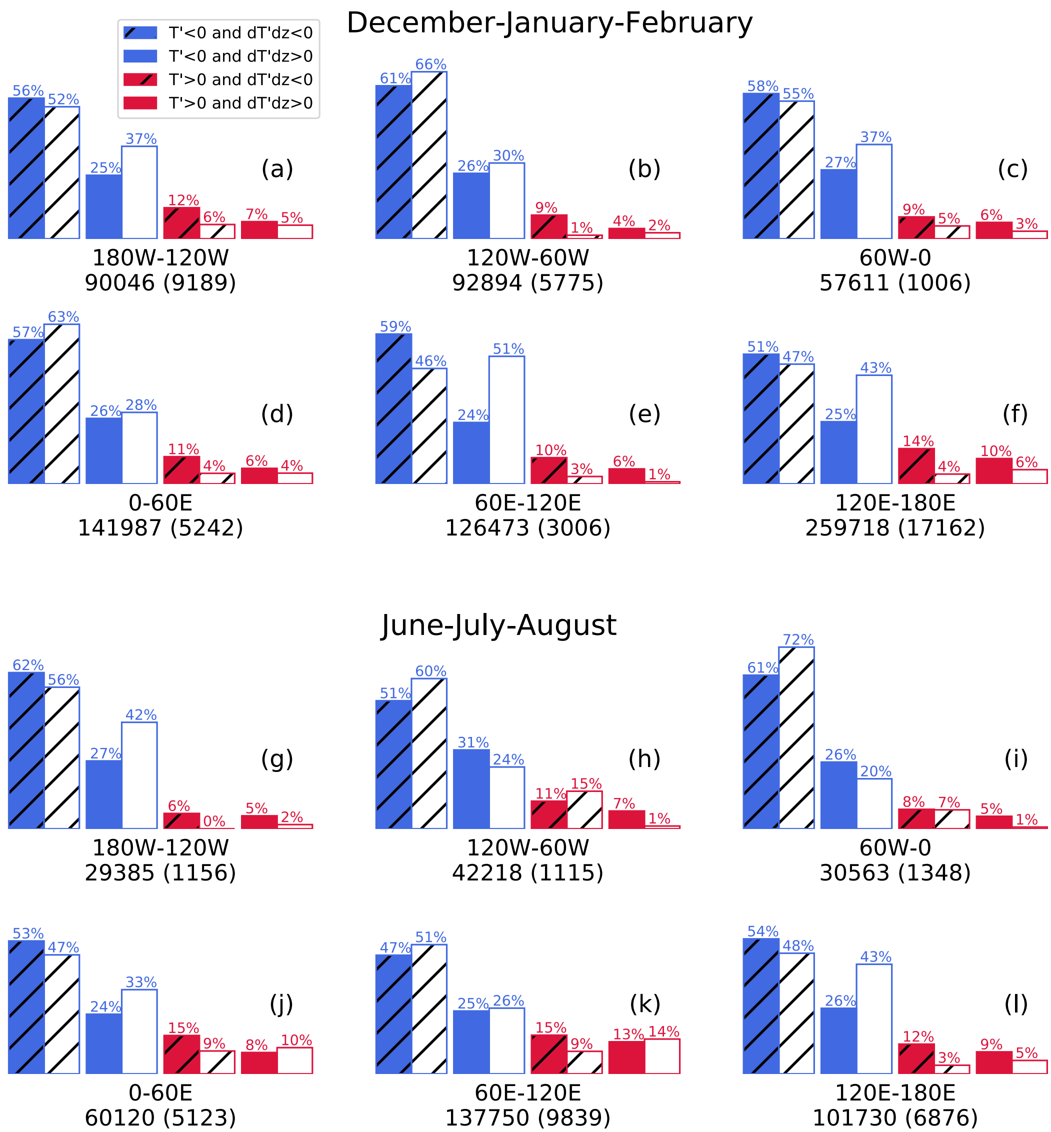

Figure 4. Same as Figure 3(a) except for different longitudinal belts. Plots (a)-(f) are for December-January-February and (g)-(l) are for June-July-August. Filled bars represent all TTL clouds, while unfilled bars represent only clouds above the mean tropopause of the respective longitudinal belt and season. The numbers of all cloud bins and bins above the tropopause (in parenthesis) in each longitudinal belt are labeled under each bar plot.

4.2 Composite time evolution of wave anomalies and cirrus occurrence

Since COSMIC observations are pseudo-random in time and space, it is possible to collocate CALIPSO observations to RO soundings with varying offsets in time. By binning the temperature profiles according to the time offsets, we can make a

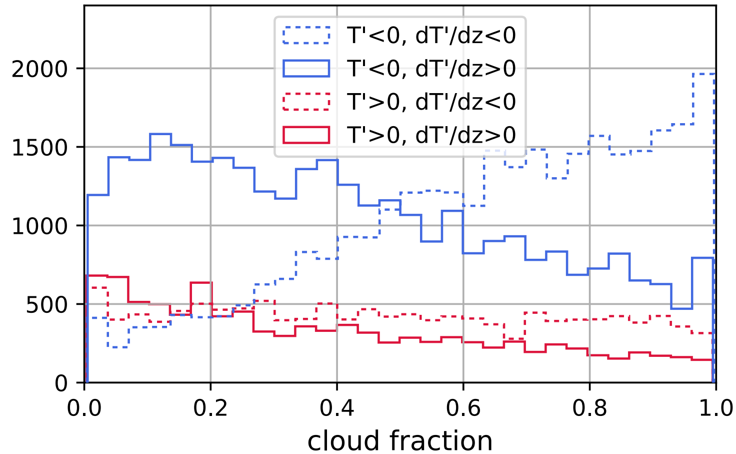

Figure 5. Distribution of cloud fraction in each gravity wave phase. Blue and red colored lines indicate the cold and warm phase, respectively, while the solid and dashed lines represent $dT'/dz > 0$ and $dT'/dz < 0$. The number of cases with cloud fractions of zero or unity are excluded.

composite showing the mean time evolution of wave anomalies relative to the cloud observation. Such an approach of creating composite time series has been used to study the thermodynamic budget before and after tropical convection (Masunaga, 2012; Masunaga and L'Ecuyer, 2014), temperature anomalies associated with tropical deep convection (Paulik and Birner, 2012), and the interaction between atmospheric dust and tropical convection (Sauter et al., 2019).

We bin RO profiles in time bins of -35, -33, ..., -1, 1, ..., 33, 35 hours relative to the CALIPSO observations, where a negative value indicates that the collocated RO profiles precede the CALIPSO overpass. The composites of T', dT'/dz, and buoyancy frequency N^2 anomaly for all collocations in 2007 to 2013 are shown in Figure 6. In making these composites we only includes clouds with cloud base of at least 14.5 km to ensure that the included clouds are TTL clouds (instead of, for example, convection) Also, for statistical testing, we need the RO profiles used in each time bin to be unique. For this reason, only the CALIPSO footprint spatially closest to the RO profile is used. If this is not done, then the same RO profile may be reused several times since there are usually multiple CALIPSO footprints collocated to one RO profile as shown in Figure 2.

In Figure 6(a), the strongest cold anomaly is found close to the cloud top and is coldest near hour 0. The cold anomaly contour with value below -0.8 K lasts approximately from -12 to $+6$ hours, and migrates downward with time consistent with the property of gravity and Kelvin waves with upward group velocity. The alternating cold-warm anomaly at heights of 2 to 6 km should be due to the diurnal tide (Zeng et al., 2008; Pirscher et al., 2010) since we are compositing only on nighttime data from CALIPSO which always crosses the equatorial region at similar local times. The number of samples in each time bin (Figure 6(c)) has a 12-hour periodicity mainly due to Metop-A/B. When only using COSMIC observations to reproduce Figure 6(a), (b),and (d), the anomaly patterns are largely the same so the periodicity does not affect the composites.

It is noteworthy that the mean cold anomaly is centered near the cloud top and not within the cloud. This results in a dipole structure in dT'/dz (Figure 6(b)) and buoyancy frequency anomaly (Figure 6(d)) with positive anomalies just above the cloud top and negative anomalies below. This structure shows that the inside of clouds (below cloud top) is likely to have negative dT'/dz, consistent with the finding by K16 and Figure 3 that a majority of clouds are found in Phase 1. Although this structure implies weakened stability (negative N^2 anomaly) inside the cloud, it is unclear whether this decreased stability has connections to cloud formation or maintenance. Since negative dT'/dz also corresponds to upward vertical motion anomalies (assuming that these anomalies are from gravity waves), their effects are difficult to separate .

A prediction of P18 is that the ice sedimentation velocity is comparable to the gravity wave vertical phase speed. In Figure 6, the descent rate of the cold anomaly within -12 to $+6$ hours is about 1 km over 18 hours. Assuming a spherical ice crystal with radius of 15 μm and ambient temperature of 200 K, P18's equation (20) (valid for radius in 5-100 μm) yields a sedimentation velocity of ~2cm/s. This corresponds to a displacement of ~1.3 km over 18 hours, which is comparable to the vertical descent rate of the cold anomaly.

Figure 7 is similar to Figure 6 except the anomalies are not composited relative to the cloud top height but rather on height above mean sea level. In this composite, there are cold anomalies at TTL altitudes but the magnitude is weaker than that of Figure 6. This leads to weak anomalies in dT'/dz (Figure 7(b)) and N^2 (not shown). Based on these results we suggest that gravity wave anomalies in Figure 6 are physically significant and have a close association with the vertical position of TTL cloud tops.

P18 argues that the upward vertical velocity in Phase 1 slows down the descent of ice crystal and tends to suspend them inside Phase 1. Since these composites depicts a downward propagation of wave anomalies, it is of interest to investigate whether the phase propagation of gravity waves is associated with a downward migration of clouds. We can explore this possibility through a compositing technique similar to the one employed above. Instead of centering on the CALIPSO footprint, we center on the time of RO sounding, and use the CALIPSO cloud product to calculate the cloud frequency in each 2-hour time bin. In addition, instead of compositing relative to cloud top height, we composite on the altitude of the *local* minima or maxima of T'. A schematic of this compositing approach is given in Figure 8.

In the example shown in Figure 8(a), at day i there is a collocated RO sounding that occurred within 100 km of the CALIPSO footprint but Δt_i hours after. The position of the cloud top and base (solid and dashed magenta lines) is evaluated relative to a local T' minimum. Since the CALIPSO overpass occurred before this RO profile, in the compositing (shown in Figure 8(b)) the observed cloud position is used to calculate the cloud fraction at Δt_i hours *before* the RO sounding. The cloud fractions are calculated on a grid of 50-m height and 2-hour time bins. For the collocation pair in Figure 8(a), the cloud fraction in the time bin corresponding to $t = -\Delta t_i$ is calculated according to how much each vertical bin overlaps with the interval $[h_i^{(b)}, h_i^{(t)}]$. If the collocated CALIPSO footprint has no clouds with base above 14.5 km, cloud fractions of zero are still binned in the appropriate time bin at all heights. Since any RO profile most likely has multiple local minima, the binning of cloud fraction is repeated for each local minimum in a T' profile. The exact same procedure is conducted for local maxima to create a separate cloud frequency composite. To focus on TTL clouds we only include clouds with base at or above 14.5 km. Also, we only consider local T' extrema within 14.5 to 18.5 km since a majority of TTL clouds are inside this height range.

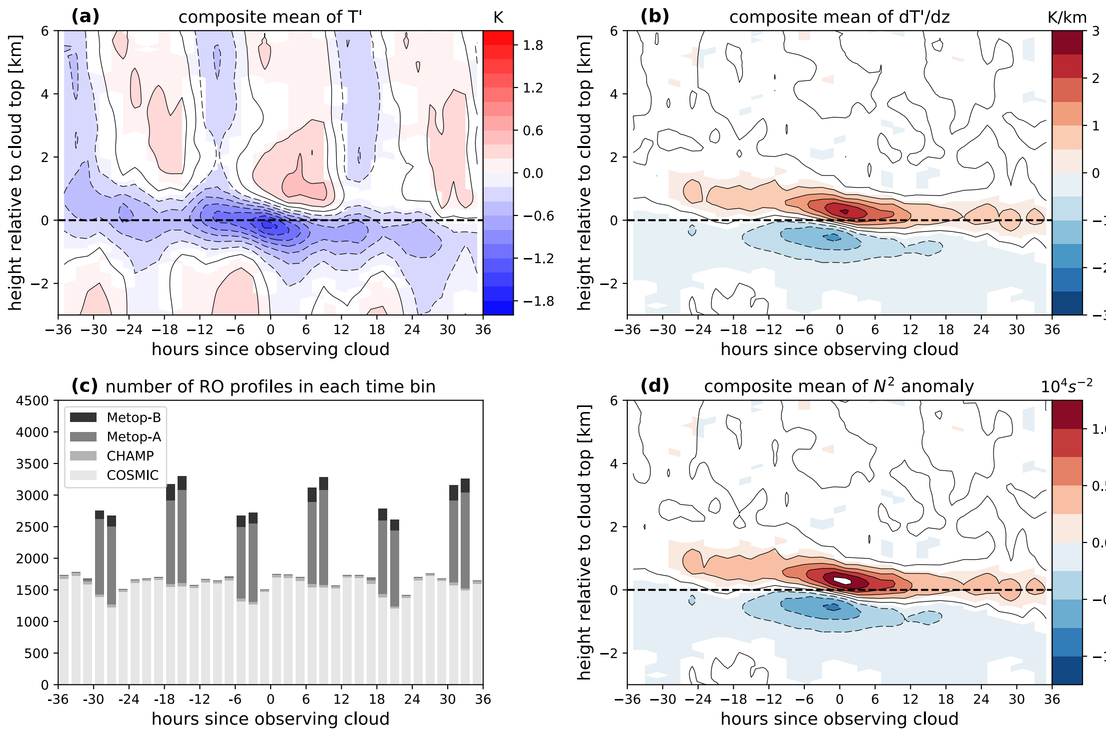

Figure 6. Composite of (a) T', (b) dT'/dz, and (d) buoyancy frequency N^2 anomaly in height coordinate relative to cloud top. Colored contours in these three plots are at or above the 95% significance level according to the Student's t-test. Solid (dashed) contours represent positive (negative) anomalies and are at the same levels as the colored contours. The abscissa denotes the time offset between the CALIPSO observation and RO sounding. Plot (c) shows the number of unique RO profiles in each 2-hour time bin used to calculate the composites.

The composites of cloud frequency made this way, shown in Figure 9(a)-(c) and (d)-(f), can then be interpreted as the probability of finding clouds in the vicinity of local T' minima or maxima, respectively. The shown values represent the mean cloud fraction in each time-height bin. Each column is produced from a different subset of T' extrema based on magnitude ($|T'| > 0.5$, 1.0, or 1.5 K). Beneath the vertical position of $min(T')$ (Figure 9(a)-(c)) we find a lobe of enhanced cloud frequency and this becomes more evident as $min(T')$ decreases. Likewise, in the vicinity of $max(T')$ (Figure 9(d)-(f)) the cloud frequency is reduced, and this reduction also shows dependence on the magnitude of $max(T')$. In both cases, the increased or decreased cloud frequency display a downward trend consistent with the expectation that gravity wave phases propagate downward with time. We devise a way to extract the cloud frequency anomaly associated with these patterns; the method and the statistical testing are detailed in the Appendix. To summarize the method briefly, we produce a background cloud frequency and compare it the pattern showns in Figure 9(a)-(c) and (d)-(f) to find statistically significant values through the Kolmogorov-Smirnov test (K-S test) (Hollander et al., 2015).

Panels (g)-(i) of Figure 9 are the anomalies associated with $min(T')$, and similarly panels (j)-(l) show the anomalies associated with $max(T')$. Colored portions of the contour denote regions with $p < 0.05$ (95% confidence) as estimated from the K-S

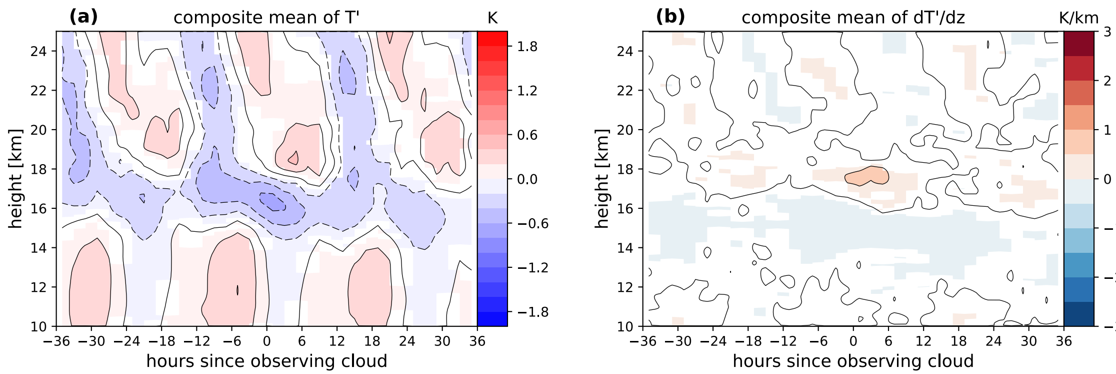

Figure 7. Composites of (a) T' and (b) dT'/dz based on height above mean sea level (instead of height coordinate relative to cloud top as in Figure 6). Colored contours are at or above the 95% significance level according to the Student's t-test. Contour levels are identical to Figure 6.

test. In these anomaly patterns it is confirmed that there is enhanced cloud occurrence below $min(T')$, and, in addition, a weak reduction of cloud occurrence above it. For the subset of $min(T') < -0.5$, the positive cloud frequency anomaly peaks at 3% whereas for $min(T') < -1.5$ it peaks at 6%. The anomaly patters due to $max(T')$ also exhibit a dipole structure with negative anomalies centered on the altitude of $max(T')$ and a weak positive anomaly below. Panels (j)-(l) also suggests a dependence of cloud frequency anomaly on the magnitude of $max(T')$, although the variation is not as large compared to that of $min(T')$. Both positive/negative anomalies associated with $min(T')$/$max(T')$ tend to migrate downward in time, although this trend is slightly more apparent in the enhanced cloud occurrence of $min(T')$.

One difference between $min(T')$ and $max(T')$ is that the positive anomalies in $min(T')$ occur below the altitude of $min(T')$ while the negative anomalies in $max(T')$ are centered on it. Most of the enhanced cloud occurrence occurs inside Phase 1, and Phase 2 actually tends to have a negative cloud occurrence anomaly. Although the predictions of P18 suggests that it may be more likely to find clouds in Phase 2 under low background RH_i, this global analysis suggests that on average the role of Phase 1 in facilitating TTL clouds is dominant.

4.3 Comparison to P18

P18 suggests that (1) ice crystals within a confined range of r_e are suspended in Phase 1, and (2) for low background relative humidity with respect to ice (RH_{ib}), the ~~confinement in~~ region of confinement may overlap with both Phase 1 ~~may be positioned~~ and 2, with its center still inside Phase 1 but closer to Phase 2. These two features are depicted in their Figure 2. To evaluate whether these predictions are consistent with satellite observations, we examine r_e and RH_{ib} in observations to see whether these quantities exhibit any correlations to clouds in each gravity wave phase. Although here we present analysis motivated by P18, we note that their study assumes no background wind shear in their derivations and simulations.

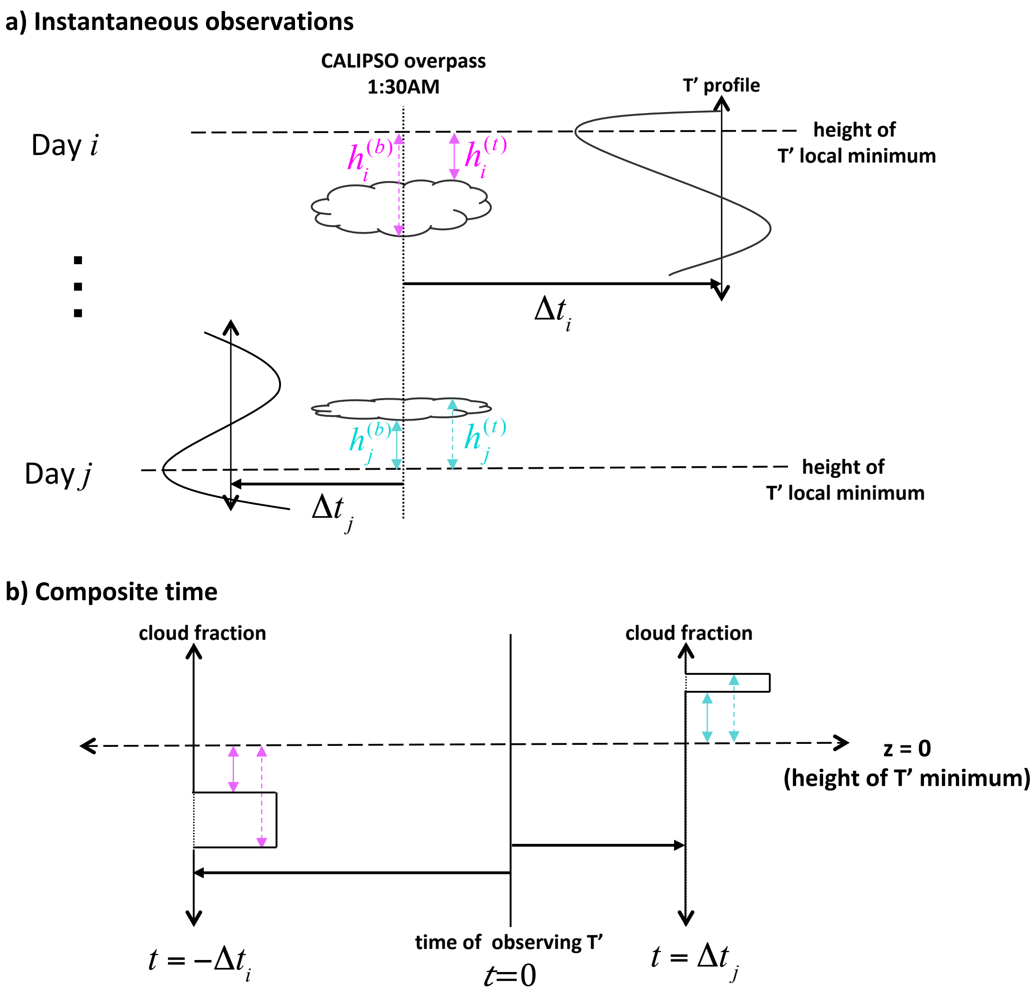

Figure 8. Schematic for creating the composite temporal evolution of cloud fraction with respect to T' minima. In this example, as shown in (a), during day i there is a collocated pair of CALIPSO and RO observations. The RO observation occurs Δt_i hours after that of CALIPSO, and the vertical distance between the height of local T' minimum and the cloud top and base is depicted by the dashed and solid magenta lines, respectively, with lengths $h_i^{(t)}$ and $h_i^{(b)}$. In the temporal compositing (b), in the time bin corresponding to Δt_i hours before observing T', the cloud fraction is binned according to how much each vertical bin overlaps with the interval $[h_i^{(b)}, h_i^{(t)}]$. The same procedure is carried out for the collocated pair at day j. Also see text for explanation.

Figure 10 shows normalized distributions of r_e in the four wave phases as well as their ~~mean and standard deviation~~means and standard deviations. These distributions only contain nighttime 2C-ICE data, since the information toward thin cirrus are mostly from lidar backscatter. Clouds above 17.5 km were omitted in this plot due to the low samples (~0.6% of all TTL clouds). ~~The distributions for all phases are very similar regardless of height. In~~ For clouds within 14.5 ~~–15.5 and 15.5–16.5~~

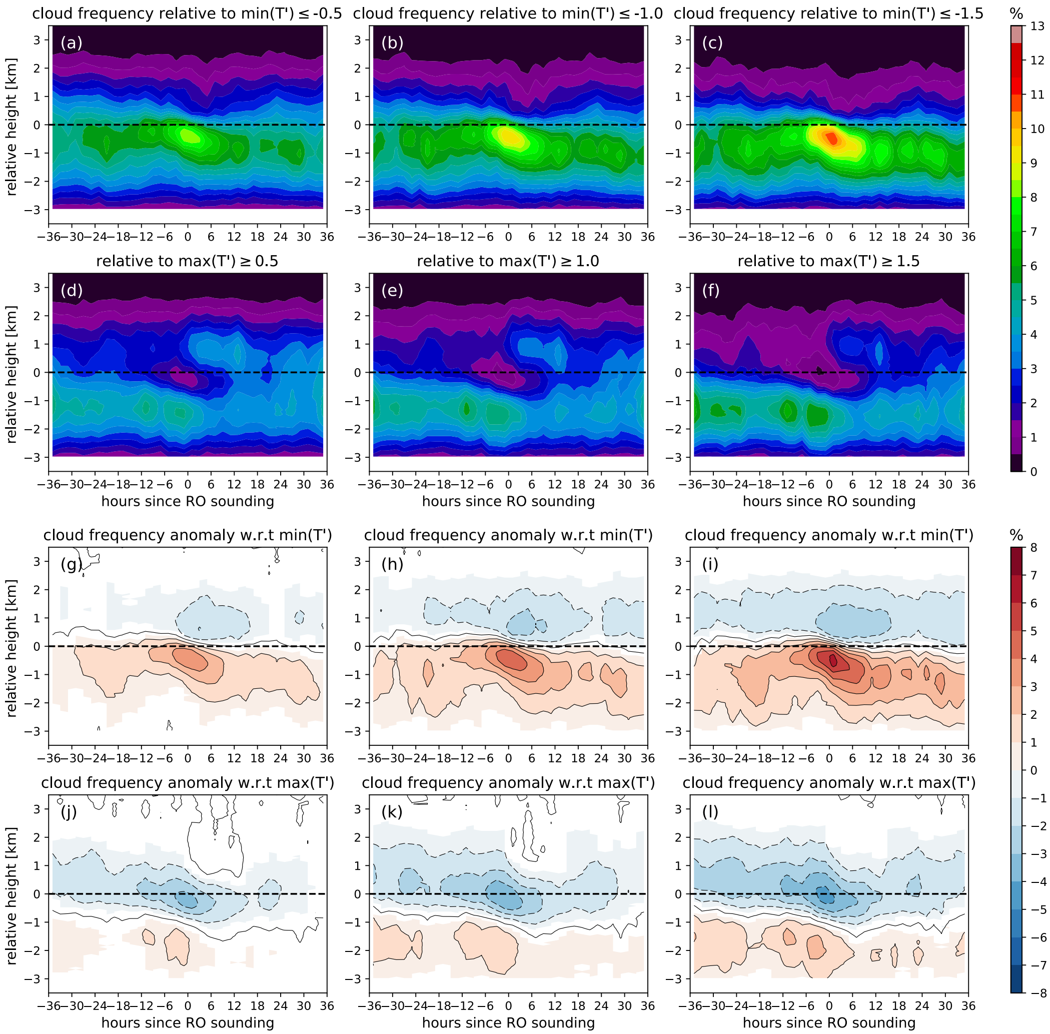

Figure 9. Composite of cloud frequency with respect to local minima (first row; panels (a)-(c)) or maxima (second row; panels (d)-(f)) of T'. The columns correspond to composites made from subsets of T' extrema with magnitudes greater or equal to 0.5 K (left column), 1.0 K (middle), and 1.5 K (right). Dashed horizontal lines indicate the position of the local T' extrema. The third row (g)-(i) and fourth rows (j-(l) are the cloud frequencies anomalies associated with cold or warm anomalies, respectively. Contours in the bottom two rows are at intervals of 1% (dashed negative), matching the filled color contours which show values at or above the 95% significance level.

~~km~~ – 16.5 km (Figure 10(a)), the r_e distribution of Phase 1 has a peak near 16 μm. Above 16.5 km (Figure 10(b)) this peak is not evident, but the Phase 1 distribution has higher values around 15 μm and lower values between 20 to 25 μm, slightly differentiating Phase 1 from the other phases. ~~The~~ In (a) and (b) the mean r_e of Phase 1 is lower than all other three phases~~at all vertical layers~~, but the differences are small. ~~Also, Phase 4 consistently has the largest~~

In Figure 10 (c) and (d) we examine two regions that are likely to be influenced by convection as inferred from Figure 4. One may have expected these regions to have more convectively detrained clouds and therefore larger mean r_e, but this is not observed here; the mean r_e ~~.~~ in (c) tends to be larger than (a) and (b) but this is not the case for (d). The influence of convection on r_e is not obvious, though we see that the r_e distributions of Phase 3 tend to resemble those of Phase 1 in these regions/seasons. The r_e distributions in (c) are notably wider (i.e. higher standard deviation) than the other categories, but the cause of this is not known.

In summary, our analysis on r_e shows that for the entire TTL (Figure 10 (a) and (b)), the observed characteristics of r_e ~~found here are qualitatively consistent~~ shows qualitative consistency with P18's findings, as Phase 1 tends to have slightly larger numbers of ice particles localized around a certain r_e value. ~~However we~~ On the other hand, the influence of convection is not apparent. We note that retrieving cloud properties of thin cirrus has large uncertainties and more research is needed to explore the r_e distribution in gravity waves phases using a variety of observations and models.

As discussed in Section 4.1, K16 found that in the 2011 and 2013 flight legs over the Eastern Pacific there were slightly more clouds in Phase 2 than Phase 1, whereas in the 2014 flights over the Western Pacific a majority of clouds were in Phase 1. P18 argues that this may be due to the relatively low RH_{ib} characteristic of the TTL over the Eastern Pacific. P18 solved a simplified set of equations describing the interaction between gravity wave perturbations and ice particle growth/sedimentation. Comparison of their solution using values of $RH_{ib} = 0.85$ or 0.63 (to represent Western and Eastern Pacific, respectively) showed that the former results in the ice crystals being suspended in Phase 1 where in the latter ice particles were situated closer ~~Phase~~ to the T minimum so that ice crystals were moving around between Phase 1 and 2. Motivated by these results we collocate the MLS water vapor retrieval to CALISPO and RO data to evaluate whether observations suggest a similar dependence on RH_{ib}.

For each CALIPSO Cloud Profile bin identified as cloud, the collocated water vapor mixing ratio from the Aura MLS product is log-interpolated (as suggested by the product documentation) to the height of the cloud bin. To evaluate the saturation mixing ratio, we interpolate the *7-day mean temperature* to the cloud height since we are interested in the RH_{ib} instead of the actual RH_i (which would include wave influence). The Goff-Gratch equation (Goff and Gratch, 1946) is used to get the saturation vapor pressure, and subsequently the saturation mixing ratio and RH_{ib}. Then the cloud bin is binned according to RH_{ib} into bins of 0%, 50%, and then every 10% up to 180%. The first bin is wider due to the small amount of samples with very low RH_{ib}. Figure 11 shows the cloud population in each phase as a function of RH_{ib} as well as the number of cloud bins in each RH_{ib} category. Compared to the relative humidity observed during the ATTREX campaign (Jensen et al., 2017), the values in our Figure 11 tends to be high-biased. A possible cause of this is that we are estimating the relative humidity as coarse-resolution MLS mixing ratio estimates divided by the saturation mixing ratio of the mean temperature. Due to the non-linearity of the Goff-Gratch equation, the relative humidity evaluated this way will be larger than the actual average relative humidity.

Qualitatively, Figure 11 is consistent with P18 since the Phase 2 percentage is higher when RH_{ib} is below 100%. The percentage of clouds in Phase 1 also tends to increase with RH_{ib} up until RH_{ib}=100%, above which there is no appreciable trend between RH_{ib} to any of the phases. To summarize, our analysis of RH_{ib} is consistent with P18's findings, while the results pertaining to r_e remain ambiguous.

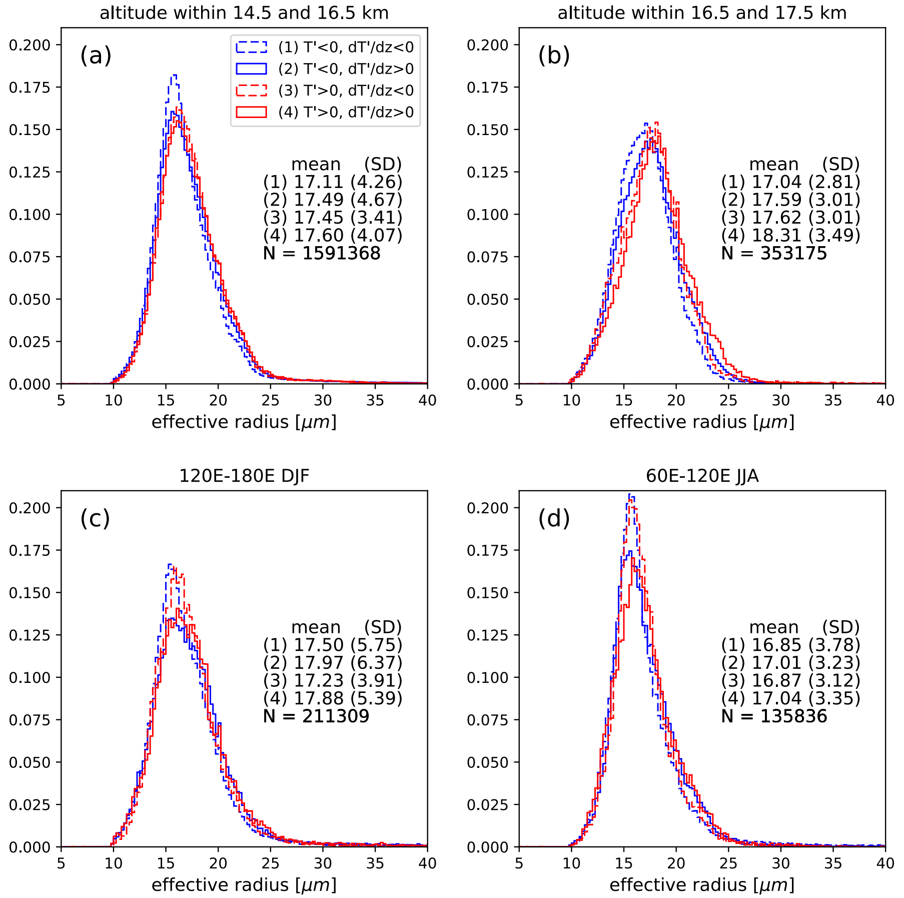

Figure 10. Normalized density function of r_e in each gravity wave phase for clouds within (a) ~~all~~ altitudes of ~~TTL and~~ 14.5 to 16.5 km, (b) ~~-~~16.5 to 17.5 km, (c) 120°E to 180°E in December-January-February, and (d) ~~1-km vertical layers~~60°E to 120°E in June-July-August. The mean and standard deviation (SD) of r_e in each phase and the total number of r_e samples (N) are denoted in the legend.

5 Conclusions

This study uses multiple satellite datasets to evaluate the influence of gravity wave perturbations on TTL cirrus clouds. With a focus on understanding the role of dT'/dz, the vertical gradient of the gravity wave temperature perturbation T', we extract T' and dT'/dz from RO observations and collocate them to clouds observed by CALIPSO and 2C-ICE to understand cloud occurrence and characteristics in distinct wave phases. Similar to the results of K16, we find that the phase where T' and dT'/dz are both negative (Phase 1) is most frequently occupied by TTL clouds. The second most populous phase is where $T' < 0$ and $dT'/dz > 0$ (Phase 2), followed by where $T' > 0$ and $dT'/dz < 0$ (Phase 3) and then $T' > 0$ and $dT'/dz > 0$ (Phase 4). We show that this relation among the four phases is more or less invariant with height or longitude.

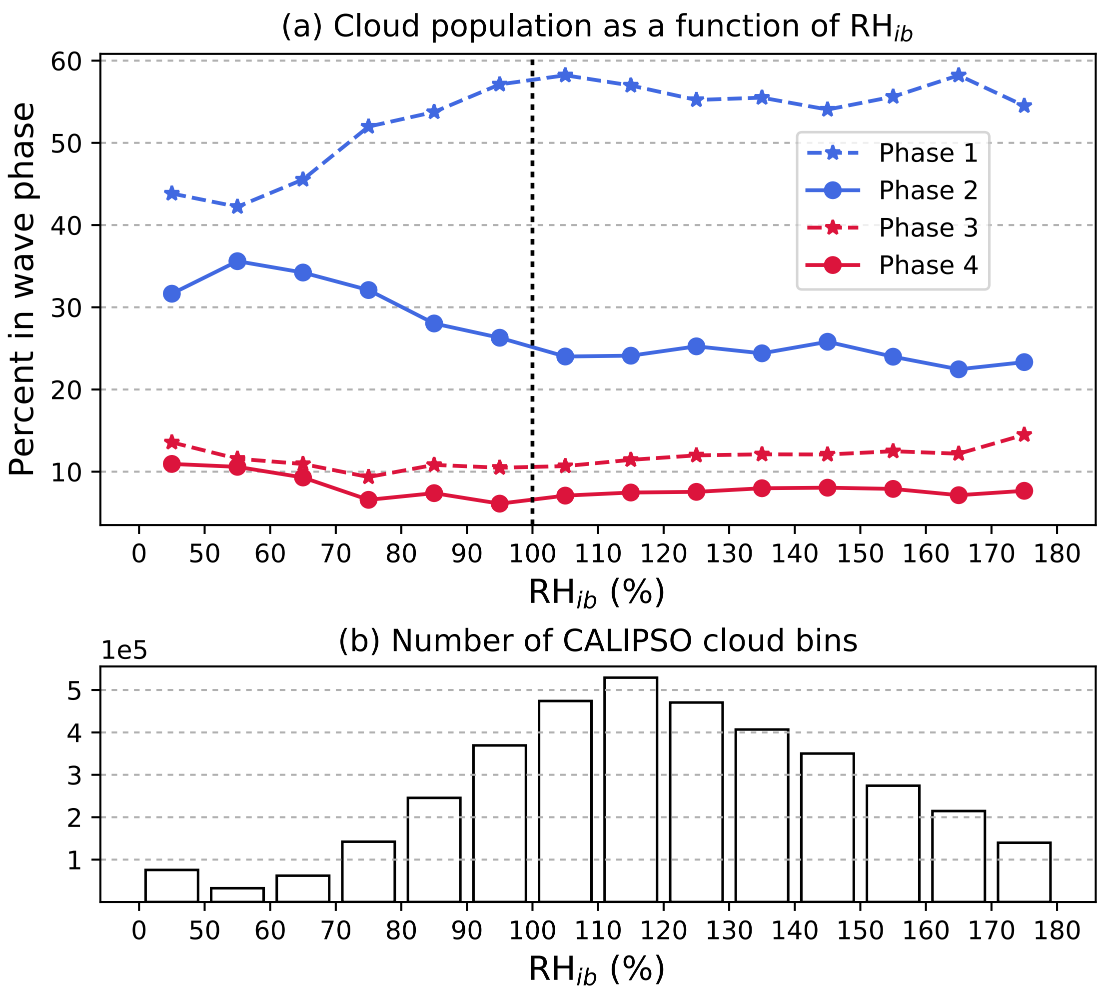

Figure 11. (a) Percentage of TTL clouds inside each wave phase as a function of background relative humidity with respect to ice (RH_{ib}). (b) Number of CALIPSO Cloud Profile bins in each RH_{ib} category.

A mean view of the temporal evolution of wave anomalies with respect to clouds is constructed by taking advantage of RO's pseudo-random distribution in time and space. We collocate CALIPSO cloud observations to RO soundings that occur before and after the CALIPSO observation, and by averaging a large number of observations with different time separations, a composite time series of wave anomalies is presented. These composites show that, on average, the strongest cold anomaly due to gravity waves tends to be centered on the height of cloud top, and this cold anomaly descends with time consistent with the downward phase propagation of gravity and Kelvin waves with upward group velocity.

In the cloud frequency composites made with respect to local T' minima or maxima, we find that the decrease of cloud probability in the warm phase does not show clear dependence on the sign of dT'/dz. This is distinct from the cold phase, where cloud probability is increased mainly below $min(T')$ where dT'/dz is negative. Together with existing studies, this result adds support to the idea that Phase 1 facilitates cloud formation and/or maintenance. Although the downward migration of the increased cloud frequency may be due to ice sedimentation, this is unlikely to be the case for the decreased cloud frequency associated with the warm phase. Hence the downward migration of increased/decreased cloud frequency in the temporal composites is most likely due to waves with downward phase propagation. We also show that the positive or negative cloud frequency anomalies strengthen with increasing magnitude of T' minima or maxima, giving evidence on a global scale that the wave amplitude is connected to the probability of cloud occurrence.

Finally, using satellite estimates of r_e from 2C-ICE we assess the predictions of P18 which implies that one may observe a narrower distribution ice crystal effective radius inside Phase 1. Their conclusion that the background relative humidity with respect to ice affects the vertical position of clouds is also evaluated here by using RH_{ib} based on the Aura MLS H_2O product. Among all phases, r_e are distributed similarly but the distribution of Phase 1 had a notably sharper peak and than the other three phases and also a slightly smaller mean r_e. The partitioning of cloud population among the four phases showed clear dependence on RH_{ib}, with Phase 1's cloud population increasing with RH_{ib} up until RH_{ib}=100%. Overall, our satellite-based analysis show qualitative consistency with the results of P18.

This study adds to the literature showing that Phase 1 has a distinct connection to TTL clouds. The findings of K16, based on aircraft data limited to specific regions and time span, have been extended by our study which shows that the large amount of clouds in Phase 1 is a general characteristic of the TTL. Based on our composite analysis using satellite data spanning seven years (2007–2013), the connection between wave anomalies and cloud occurrence is evident: cold anomalies are associated with the position of cloud top, and T' amplitudes influence the increase or decrease in cloud frequency. The purpose of constructing composite temporal evolution by piecing together collocated temperature and cloud observations is an attempt to study processes occurring on a timescale typically unobserved by satellites. Although the resulting composites are not true time series, the anomaly patterns are consistent with wave propagation and enhances our understanding of how waves are connected to TTL clouds. It should be noted that although the composite technique shows a clear connection between wave anomalies and clouds, the technique is stationary in space; it does not follow the position of clouds (moved by the background flow) nor the wave phase (moved as it propagates).

Due to the spatial and vertical resolution of the RO technique, the waves analyzed here have relatively large vertical wavelengths and low frequencies. The vertical wavelength inferred from the anomalies in our composites is about 3 km. Dzambo et al. (2019) showed that the power spectrum of TTL gravity waves tend to peak at wavelengths of around 4–5 km, though at 3 km there is still considerable power (their Figure 1). These wavelengths are all resolvable by RO, so it can be assumed that this analysis has included a large part of the TTL gravity wave spectrum. Nevertheless, it remains to be explored whether the Phase 1 of high-frequency waves are also distinct from other phases. Also, possible explanations for Phase 1 favoring clouds remain an open question. Since negative dT'/dz corresponds to a upward wind anomaly as well as weakened stability, it remains to be determined whether one has a stronger role in promoting cloud formation.

Data availability. The atmPrf radio occultation dataset can be obtained from the COSMIC Data Analysis and Archive Center (https://cdaac-www.cosmic.ucar.edu/). The Aura MLS Level 2 H_2O product is available from the Goddard Earth Sciences Data and Information Services Center (https://disc.gsfc.nasa.gov), and the 2C-ICE CloudSat/CALIPSO product is available on the CloudSat Data Processing Center (www.cloudsat.cira.colostate.edu). The CALIPSO Level 2 Cloud Profile and Cloud Layer products are hosted on the NASA Atmospheric Science Data Center (https://eosweb.larc.nasa.gov).

Appendix A: Calculation of background cloud frequency for Figure 9

The cloud frequency composites in the top two rows of Figure 9 are made using the altitude of the T' extrema as the zero height. To generate a composite where the vertical positon of T' extrema has no relationship with cloud top/base height, for each T' extremum we generate a random altitude using uniform distribution $unif(14.5, 18.5)$ and make a separate cloud frequency time-height composite with the random altitude as zero height. The resulting cloud frequency height-time distribution is regarded as the ’background’ distribution. The difference between this background and the cloud frequency composites in Figure 9 (a)-(f) are then the anomalies associated with local T' minimum or maximum. The anomalies derived in this way are shown in Figure 9 (g)-(l).

The distribution of cloud fraction in each time-height bin is similar to those shown in Figure 5 and therefore is not normal, so the Student’s t-test cannot be used for statistical testing. We use the two-sided two-sample Kolmogorov-Smirnov test which does not make any assumptions about the data distributions. This test can be used to evaluate whether two discrete probability distributions differ from each other. The null hypothesis is that the cloud frequency pattern composited on T' minima/maxima (first/second row of Figure 9) is not different than the randomly generated ’background’ cloud frequency pattern.

Author contributions. KC designed and performed the study with suggestions from TL. Both authors contributed to the writing of this article.

Competing interests. The authors declare no conflicts of interest.

Acknowledgements. This study was supported by the NASA Earth and Space Sciences Fellowship 80NSSC17K0384. We thank Sergey Sokolovskiy and Zhen Zeng for comments regarding the usage of radio occultation data and William Read regarding the Aura MLS H_2O product.

References

Alexander, S. P., Tsuda, T., Kawatani, Y., and Takahashi, M.: Global distribution of atmospheric waves in the equatorial upper troposphere and lower stratosphere: COSMIC observations of wave mean flow interactions, Journal of Geophysical Research Atmospheres, 113, 1–18, https://doi.org/10.1029/2008JD010039, 2008.

Anthes, R. A., Bernhardt, P. A., Chen, Y., Cucurull, L., Dymond, K. F., Ector, D., Healy, S. B., Ho, S.-P., Hunt, D. C., Kuo, Y.-H., Liu, H., Manning, K., McCormick, C., Meehan, T. K., Randel, W. J., Rocken, C., Schreiner, W. S., Sokolovskiy, S. V., Syndergaard, S., Thompson, D. C., Trenberth, K. E., Wee, T.-K., Yen, N. L., and Zeng, Z.: The COSMIC/FORMOSAT-3 Mission: Early Results, Bulletin of the American Meteorological Society, 89, 313–334, https://doi.org/10.1175/BAMS-89-3-313, http://journals.ametsoc.org/doi/10.1175/BAMS-89-3-313, 2008.

Banerjee, A., Chiodo, G., Previdi, M., Ponater, M., Conley, A. J., and Polvani, L. M.: Stratospheric water vapor: an important climate feedback, Climate Dynamics, 0, 1–14, https://doi.org/10.1007/s00382-019-04721-4, https://link.springer.com/article/10.1007{%}2Fs00382-019-04721-4, 2019.

Deng, M., Mace, G. G., Wang, Z., and Paul Lawson, R.: Evaluation of several A-Train ice cloud retrieval products with in situ measurements collected during the SPARTICUS campaign, Journal of Applied Meteorology and Climatology, 52, 1014–1030, https://doi.org/10.1175/JAMC-D-12-054.1, 2013.

Deng, M., Mace, G. G., Wang, Z., and Berry, E.: Cloudsat 2C-ICE product update with a new Ze parameterization in lidar-only region, Journal of Geophysical Research, 120, 12,198–12,208, https://doi.org/10.1002/2015JD023600, 2015.

Dzambo, A. M., Hitchman, M. H., and Chang, K. W.: The influence of gravity waves on ice saturation in the tropical tropopause layer over darwin, Australia, Atmosphere, 10, https://doi.org/10.3390/ATMOS10120778, 2019.

Foelsche, U., Scherllin-Pirscher, B., Ladstädter, F., Steiner, A. K., and Kirchengast, G.: Refractivity and temperature climate records from multiple radio occultation satellites consistent within 0.05%, Atmospheric Measurement Techniques, 4, 2007–2018, https://doi.org/10.5194/amt-4-2007-2011, 2011.

Fujiwara, M., Iwasaki, S., Shimizu, A., Inai, Y., Shiotani, M., Hasebe, F., Matsui, I., Sugimoto, N., Okamoto, H., Nishi, N., Hamada, A., Sakazaki, T., and Yoneyama, K.: Cirrus observations in the tropical tropopause layer over the western Pacific, Journal of Geophysical Research Atmospheres, 114, 1–23, https://doi.org/10.1029/2008JD011040, 2009.

Goff, J. A. and Gratch, S.: Low-pressure properties of water from -160 to 212 °F, in: Transactions of the American Society of Heating and Ventilating Engineers, New York, pp. 95–122, 1946.

Highwood, E. J. and Hoskins, B. J.: The tropical tropopause, Quarterly Journal of the Royal Meteorological Society, 124, 1579–1604, https://doi.org/10.1002/qj.49712454911, http://doi.wiley.com/10.1002/qj.49712454911, 1998.

Hollander, M., A. Wolfe, D., and Chicken, E.: Nonparametric Statistical Methods, Wiley Series in Probability and Statistics, Wiley, third edit edn., https://doi.org/10.1002/9781119196037, https://onlinelibrary.wiley.com/doi/book/10.1002/9781119196037, 2015.

Holton, J. R., Haynes, P. H., McIntyre, M. E., Douglass, A. R., Rood, R. B., and Pfister, L.: Stratosphere-troposphere exchange, Reviews of Geophysics, 33, 403, https://doi.org/10.1029/95RG02097, http://doi.wiley.com/10.1029/95RG02097, 1995.

Immler, F., Krüger, K., Tegtmeier, S., Fujiwara, M., Fortuin, P., Verver, G., and Schrems, O.: Cirrus clouds, humidity, and dehydration in the tropical tropopause layer observed at Paramaribo, Suriname (5.8°N, 55.2°W), Journal of Geophysical Research Atmospheres, 112, 1–14, https://doi.org/10.1029/2006JD007440, 2007.

Jensen, E. J., Diskin, G., Lawson, R. P., Lance, S., Bui, T. P., Hlavka, D., McGill, M., Pfister, L., Toon, O. B., and Gao, R.: Ice nucleation and dehydration in the Tropical Tropopause Layer, Proceedings of the National Academy of Sciences, 110, 2041–2046, https://doi.org/10.1073/pnas.1217104110, http://www.pnas.org/content/110/6/2041http://www.pnas.org/cgi/doi/10.1073/pnas.1217104110, 2013.

Jensen, E. J., Thornberry, T. D., Rollins, A. W., Ueyama, R., Pfister, L., Bui, T., Diskin, G. S., Digangi, J. P., Hintsa, E., Gao, R. S., Woods, S., Lawson, R. P., and Pittman, J.: Physical processes controlling the spatial distributions of relative humidity in the tropical tropopause layer over the Pacific, Journal of Geophysical Research, 122, 6094–6107, https://doi.org/10.1002/2017JD026632, 2017.

Kim, J.-E., Alexander, M. J., Bui, T. P., Dean-Day, J. M., Lawson, R. P., Woods, S., Hlavka, D., Pfister, L., and Jensen, E. J.: Ubiquitous influence of waves on tropical high cirrus clouds, Geophysical Research Letters, 43, 5895–5901, https://doi.org/10.1002/2016GL069293, http://doi.wiley.com/10.1002/2016GL069293, 2016.

Kursinski, E. R., Hajj, G. A., Schofield, J. T., Linfield, R. P., and Hardy, K. R.: Observing Earth's atmosphere with radio occultation measurements using the Global Positioning System, Journal of Geophysical Research: Atmospheres, 102, 23 429–23 465, https://doi.org/10.1029/97JD01569, http://doi.wiley.com/10.1029/97JD01569, 1997.

Lambert, A., Read, W. G., Livesey, N. J., Santee, M. L., Manney, G. L., Froidevaux, L., Wu, D. L., Schwartz, M. J., Pumphrey, H. C., Jimenez, C., Nedoluha, G. E., Cofield, R. E., Cuddy, D. T., Daffer, W. H., Drouin, B. J., Fuller, R. A., Jarnot, R. F., Knosp, B. W., Pickett, H. M., Perun, V. S., Snyder, W. V., Stek, P. C., Thurstans, R. P., Wagner, P. A., Waters, J. W., Jucks, K. W., Toon, G. C., Stachnik, R. A., Bernath, P. F., Boone, C. D., Walker, K. A., Urban, J., Murtagh, D., Elkins, J. W., and Atlas, E.: Validation of the Aura Microwave Limb Sounder middle atmosphere water vapor and nitrous oxide measurements, Journal of Geophysical Research, 112, D24S36, https://doi.org/10.1029/2007JD008724, http://doi.wiley.com/10.1029/2007JD008724, 2007.

Livesey, N. J., Read, W. G., Wagner, P. A., Froidevaux, L., Lambert, A., Manney, G. L., Valle, L. F. M., Pumphrey, H. C., Santee, M. L., Schwartz, M. J., Wang, S., Fuller, R. A., Jarnot, R. F., Knosp, B. W., Martinez, E., and Lay, R. R.: Version 4.2 x Level 2 data quality and description document, JPL D-33509 Rev. C, Jet Propulsion Laboratory, https://mls.jpl.nasa.gov/data/v4-2{_}data{_}quality{_}document.pdf, 2017.

Masunaga, H.: A Satellite Study of the Atmospheric Forcing and Response to Moist Convection over Tropical and Subtropical Oceans, Journal of the Atmospheric Sciences, 69, 150–167, https://doi.org/10.1175/JAS-D-11-016.1, http://journals.ametsoc.org/doi/abs/10.1175/JAS-D-11-016.1, 2012.

Masunaga, H. and L'Ecuyer, T. S.: A Mechanism of Tropical Convection Inferred from Observed Variability in the Moist Static Energy Budget, Journal of the Atmospheric Sciences, 71, 3747–3766, https://doi.org/10.1175/JAS-D-14-0015.1, http://journals.ametsoc.org/doi/abs/10.1175/JAS-D-14-0015.1, 2014.

Paulik, L. C. and Birner, T.: Quantifying the deep convective temperature signal within the tropical tropopause layer (TTL), Atmospheric Chemistry and Physics, 12, 12 183–12 195, https://doi.org/10.5194/acp-12-12183-2012, http://www.atmos-chem-phys.net/12/12183/2012/, 2012.

Pirscher, B., Foelsche, U., Borsche, M., Kirchengast, G., and Kuo, Y.-H.: Analysis of migrating diurnal tides detected in FORMOSAT-3/COSMIC temperature data, Journal of Geophysical Research, 115, D14 108, https://doi.org/10.1029/2009JD013008, http://doi.wiley.com/10.1029/2009JD013008, 2010.

Ploeger, F., Gottschling, C., Griessbach, S., Grooß, J. U., Guenther, G., Konopka, P., Muller, R., Riese, M., Stroh, F., Tao, M., Ungermann, J., Vogel, B., and Von Hobe, M.: A potential vorticity-based determination of the transport barrier in the Asian summer monsoon anticyclone, Atmospheric Chemistry and Physics, 15, 13 145–13 159, https://doi.org/10.5194/acp-15-13145-2015, 2015.

Podglajen, A., Plougonven, R., Hertzog, A., and Jensen, E.: Impact of gravity waves on the motion and distribution of atmospheric ice particles, Atmospheric Chemistry and Physics, 18, 10 799–10 823, https://doi.org/10.5194/acp-18-10799-2018, 2018.

Ramage, C. S.: Role of a tropical “Maritime Continent” in the atmospheric circulation, Monthly Weather Review, 96, 365–370, https://doi.org/10.1175/1520-0493(1968)096<0365:ROATMC>2.0.CO;2, http://journals.ametsoc.org/doi/abs/10.1175/1520-0493{%}281968{%}29096{%}3C0365{%}3AROATMC{%}3E2.0.CO{%}3B2, 1968.

Randel, W. J. and Wu, F.: Kelvin wave variability near the equatorial tropopause observed in GPS radio occultation measurements, Journal of Geophysical Research D: Atmospheres, 110, 1–13, https://doi.org/10.1029/2004JD005006, 2005.

Read, W. G., Lambert, A., Bacmeister, J., Cofield, R. E., Christensen, L. E., Cuddy, D. T., Daffer, W. H., Drouin, B. J., Fetzer, E., Froidevaux, L., Fuller, R., Herman, R., Jarnot, R. F., Jiang, J. H., Jiang, Y. B., Kelly, K., Knosp, B. W., Kovalenko, L. J., Livesey, N. J., Liu, H.-C., Manney, G. L., Pickett, H. M., Pumphrey, H. C., Rosenlof, K. H., Sabounchi, X., Santee, M. L., Schwartz, M. J., Snyder, W. V., Stek, P. C., Su, H., Takacs, L. L., Thurstans, R. P., Vömel, H., Wagner, P. A., Waters, J. W., Webster, C. R., Weinstock, E. M., and Wu, D. L.: Aura Microwave Limb Sounder upper tropospheric and lower stratospheric H 2 O and relative humidity with respect to ice validation, Journal of Geophysical Research, 112, D24S35, https://doi.org/10.1029/2007JD008752, http://doi.wiley.com/10.1029/2007JD008752, 2007.

Sassen, K., Wang, Z., and Liu, D.: Cirrus clouds and deep convection in the tropics: Insights from CALIPSO and CloudSat, Journal of Geophysical Research Atmospheres, 114, 1–11, https://doi.org/10.1029/2009JD011916, 2009.

Sauter, K., L'Ecuyer, T. S., den Heever, S. C., Twohy, C., Heidinger, A., Wanzong, S., and Wood, N.: The Observed Influence of Tropical Convection on the Saharan Dust Layer, Journal of Geophysical Research: Atmospheres, p. 2019JD031365, https://doi.org/10.1029/2019JD031365, https://onlinelibrary.wiley.com/doi/abs/10.1029/2019JD031365, 2019.

Scherllin-Pirscher, B., Randel, W. J., and Kim, J.: Tropical temperature variability and Kelvin-wave activity in the UTLS from GPS RO measurements, Atmospheric Chemistry and Physics, 17, 793–806, https://doi.org/10.5194/acp-17-793-2017, 2017.

Schoeberl, M. R., Jensen, E. J., and Woods, S.: Gravity waves amplify upper tropospheric dehydration by clouds, Earth and Space Science, 2, 485–500, https://doi.org/10.1002/2015EA000127, http://doi.wiley.com/10.1002/2015EA000127, 2015.

Solomon, S., Rosenlof, K. H., Portmann, R. W., Daniel, J. S., Davis, S. M., Sanford, T. J., and Plattner, G.-K.: Contributions of Stratospheric Water Vapor to Decadal Changes in the Rate of Global Warming, Science, 327, 1219–1223, https://doi.org/10.1126/science.1182488, http://www.sciencemag.org/cgi/content/abstract/327/5970/1219http://www.sciencemag.org/cgi/doi/10.1126/science.1182488, 2010.

Suzuki, J., Fujiwara, M., Nishizawa, T., Shirooka, R., Yoneyama, K., Katsumata, M., Matsui, I., and Sugimoto, N.: The occurrence of cirrus clouds associated with eastward propagating equatorial n = 0 inertio-gravity and Kelvin waves in November 2011 during the CINDY2011/DYNAMO campaign, Journal of Geophysical Research Atmospheres, 118, 12 941–12 947, https://doi.org/10.1002/2013JD019960, 2013.

Von Engeln, A., Healy, S., Marquardt, C., Andres, Y., and Sancho, F.: Validation of operational GRAS radio occultation data, Geophysical Research Letters, 36, 5–8, https://doi.org/10.1029/2009GL039968, 2009.

Wickert, J., Reigber, C., Beyerle, G., König, R., Marquardt, C., Schmidt, T., Grunwaldt, L., Galas, R., Meehan, T. K., Melbourne, W. G., and Hocke, K.: Atmosphere sounding by GPS radio occultation: First results from CHAMP, Geophysical Research Letters, 28, 3263–3266, https://doi.org/10.1029/2001GL013117, http://doi.wiley.com/10.1029/2001GL013117, 2001.

Winker, D. M., Pelon, J., Coakley, J. A., Ackerman, S. A., Charlson, R. J., Colarco, P. R., Flamant, P., Fu, Q., Hoff, R. M., Kittaka, C., Kubar, T. L., Le Treut, H., Mccormick, M. P., Mégie, G., Poole, L., Powell, K., Trepte, C., Vaughan, M. A., and Wielicki, B. A.: The CALIPSO Mission, Bulletin of the American Meteorological Society, 91, 1211–1230, https://doi.org/10.1175/2010BAMS3009.1, http://journals.ametsoc.org/doi/10.1175/2010BAMS3009.1, 2010.

Zeng, Z., Randel, W., Sokolovskiy, S., Deser, C., Kuo, Y.-H., Hagan, M., Du, J., and Ward, W.: Detection of migrating diurnal tide in the tropical upper troposphere and lower stratosphere using the Challenging Minisatellite Payload radio occultation data, Journal of Geophysical Research, 113, D03 102, https://doi.org/10.1029/2007JD008725, http://doi.wiley.com/10.1029/2007JD008725, 2008.

Zeng, Z., Sokolovskiy, S., Schreiner, W. S., and Hunt, D.: Representation of vertical atmospheric structures by radio occultation observations in the upper troposphere and lower stratosphere: Comparison to high-resolution radiosonde profiles, Journal of Atmospheric and Oceanic Technology, 36, 655–670, https://doi.org/10.1175/JTECH-D-18-0105.1, 2019.